

To appear in the *Journal of Hydraulic Research*
Vol. 00, No. 00, Month 20XX, 1–33

Research paper

Numerical Investigation of Field-Scale Geysers in a Vertical Shaft

TAHER CHEGINI (IAHR Member), PhD Student, *Department of Civil and Environmental Engineering, University of Houston, Houston, Texas, United States of America*
Email: tchegini@uh.edu (author for correspondence)

ARTURO S. LEON, PH.D., P.E., D.WRE (IAHR Member), Associate Professor, *Department of Civil and Environmental Engineering, Florida International University, Miami, Florida, United States of America*
Email: arleon@fiu.edu

Geysers in Vertical Shafts

ABSTRACT

Geysers in dropshafts of sewer systems are consecutive eruptions of a mixture of gas and liquid that can attain heights of more than 30 m. The present study investigates the mechanisms and characteristics of these extreme events numerically using OpenFOAM toolbox. The numerical model is based on a compressible two-phase flow solver and was validated using experimental results available in the literature. The results showed that the geyser events occurred in the experiments can be simulated with the model in both two and three dimensions. However, applicability of the two dimensional model for modeling geysers in actual sewer systems requires further studies. Moreover, the results suggested that compressibility of air plays a critical role in the formation of geysers. The conducted numerical study provides insights into the characteristics of geysers and presents some criteria for performing efficient numerical simulations of geyser events.

Keywords: Air-water interface interactions; flows in pipes; geyser; numerical validation; OpenFOAM; sewer hydraulics

1 Introduction

Stormwater and Combined Sewer Systems are generally assemblies of near-horizontal pipes or tunnels and vertical shafts (dropshafts) which may serve as maintenance access, air ventilation or inflow passage. During extreme precipitation events, the tunnels might fill rapidly, causing surcharge of sewer systems and subsequent changes to their hydrodynamics (Yen et al., 1980). These changes influence capacity and functionality of the sewer systems and can lead to unsteady phenomena such as geyser events which are violent consecutive eruptions through dropshafts, where the strongest eruption is not the first one but few eruptions later (Leon et al., 2018). Due to the adverse effects of this phenomenon, such as infrastructure damage and pedestrian safety, geysers have been subjected to experimental and numerical studies over the past three decades.

There is yet no consensus regarding the mechanisms leading to geyser events. A number of studies have focused on the experimental reproduction of a geyser event, e.g. Vasconcelos and Wright (2005), Lewis (2011) and Cong et al. (2017). These studies explained the significant role of entrapped air pockets in horizontal pipes in the formation of geysers but failed to reproduce eruptions with characteristics similar to actual geysers in sewer systems. In particular, these studies produced spring-like eruptions, where the first eruption is the strongest eruption. A field study published in Wright et al. (2011) provided insightful observations regarding the frequency of consecutive eruptions and pressures attained during geysering events. The data presented in Wright et al. (2011) was collected from a sewer system below Interstate 35W in Minnesota. The data showed that pressure heads close to the bottom of the vertical shaft never reached the required head to push the column of water above ground level. Moreover, based on the footage of a geyser event captured on a traffic cam in Minnesota (MN Dot, 1999), each event consisted of several consecutive eruptions; a few weak ones followed by several strong eruptions.

Muller et al. (2017) and Cong et al. (2017) conducted a series of similar experiments which consisted of a vertical riser, a horizontal pipe, and a tank. They produced spring-like eruptions i.e., one strong eruption followed by rapidly decaying eruptions. Moreover, Cong et al. (2017) concluded that the occurrence of eruptions is more likely when two conditions are met; the ratio of the riser diameter to the horizontal pipe is less than 0.62 and the volume of the air pocket is larger than a certain limit which depends on the upstream head and diameter of the riser. The eruptions produced in Cong et al. (2017) and Muller et al. (2017) are substantially smaller than those achieved in actual geysers e.g., based on field observations Wright et al. (2011) reported geyser heights of about 20 m. A series of recent laboratory experiments (Leon et al., 2018) successfully reproduced geysers with heights exceeding 30 m and with characteristics resembling geysers in actual sewer systems. The results of Leon et al. (2018), details of which are discussed in the following sections, were used in the current study for validating the numerical model.

Additionally, a number of studies have focused on numerical modeling of geysers using single-phase models such as Hamam and McCorquodale (1982) and Guo and Song (1991), and two-phase

flow models e.g. [Choi et al. \(2014\)](#) and [Chan et al. \(2018\)](#). Single-phase flow models underestimate air-water interaction i.e., momentum exchange between entrapped air and water is not considered which is important in the formation of geyser ([Vasconcelos et al., 2009](#)). [Choi et al. \(2014\)](#) used a compressible solver in Star-CCM+ software package ([CD-adapco, 2012](#)) and a set of experimental data in [Vasconcelos and Wright \(2011\)](#) for studying spring-like geysers. Moreover, [Chan et al. \(2018\)](#) also used a compressible solver to perform a series of 3D simulations based on experimental results in [Cong et al. \(2017\)](#). These authors conclude that smaller riser diameter, greater upstream head and larger air pocket increase the intensity of geyser eruptions. The numerical study of these authors has the same shortcomings as those of [Cong et al. \(2017\)](#) i.e., the simulated eruptions did not have the characteristics of geysers in actual stormsewer systems.

The current study utilizes OpenFOAM ([CFD Direct, 2017](#)) to numerically investigate geysers presented in [Leon et al. \(2018\)](#). The rest of the paper is organized as follows; first, the numerical procedure including the governing equations and the solution algorithm is briefly described. Then validation of the model based on experimental data in [Leon et al. \(2018\)](#) and subsequent numerical investigations are discussed. Finally, concluding remarks are made.

2 Numerical Model

OpenFOAM offers a set of C++ libraries for solving partial differential equations and provides several solvers for CFD applications. Considering the physics of geysers, which was briefly discussed in the previous section, a compressible two-phase flow solver called `compressibleInterFoam` (CIF) was used in this study. CIF is suitable for modeling two compressible and immiscible fluids ([CFD Direct, 2017](#)).

CIF employs an interface capturing approach using a Volume Of Fluid method for simulating interactions between two fluids. In the present paper, these two phases are water and air which are denoted by w and a subscripts, respectively. The properties of fluids are calculated for the mixture of two fluids based on the volume fraction of each phase. For example, the density of the mixture is calculated using $\rho = \alpha\rho_w + (1 - \alpha)\rho_a$, where α is the volume fraction of water, and ρ_w and ρ_a represent the densities of water and air, respectively.

Moreover, the compressibility of phases can be adjusted through equations of state (EOS). In OpenFOAM, a phase can be considered as incompressible by setting the EOS to `rhoConst` i.e., the density of the phase is considered a constant. Conversely, water and air phases can be regarded as compressible by, for instance, using perfect fluid and ideal gas laws, respectively, given by

$$\rho_w = \rho_{w,0} + \frac{p}{R_w T}, \quad \rho_a = \frac{p}{R_a T}. \quad (1)$$

Where p and T are pressure and temperature of the mixture, respectively, and the other parameters are the fluids' constants which for the current study are considered as $\rho_{w,0} = 998.4 \text{ kg m}^{-3}$, $R_w = 3000 \text{ J kg}^{-1} \text{ K}^{-1}$ and $R_a = 287 \text{ J kg}^{-1} \text{ K}^{-1}$.

The conservation laws of mass, Eq. 2, momentum, Eq. 3 and energy, Eq. 4, for a homogeneous mixture are implemented in OpenFOAM as follows (e.g [Ma et al. 2016](#)):

$$\frac{\partial \rho}{\partial t} + \nabla \cdot (\rho \mathbf{U}) = 0, \quad (2)$$

$$\frac{\partial \rho \mathbf{U}}{\partial t} + \nabla \cdot (\rho \mathbf{U} \mathbf{U}) - \nabla \cdot (\mu \nabla \mathbf{U}) = \sigma \kappa \nabla \alpha - \mathbf{g} \cdot \mathbf{x} \nabla \rho - \nabla p_d, \quad (3)$$

$$\frac{\partial \rho T}{\partial t} + \nabla \cdot (\rho \mathbf{U} T) - \nabla \cdot (\alpha_t \nabla T) = - \left(\frac{\alpha}{c_{v,a}} + \frac{1 - \alpha}{c_{v,w}} \right) \left(\frac{\partial \rho K}{\partial t} + \nabla \cdot (\rho \mathbf{U} K) + \nabla \cdot (\mathbf{U} p) \right) \quad (4)$$

where \mathbf{U} is the velocity vector and κ is the curvature of the interface which is given by $\kappa = \nabla \cdot \left(\frac{\nabla \alpha}{|\nabla \alpha|} \right)$; \mathbf{g} is the gravitational acceleration vector given by $(0, 9.81, 0) \text{ m s}^{-2}$ and \mathbf{x} represents the position vector; p_d is the dynamic pressure, given by $p_d = p - \rho \mathbf{g} \cdot \mathbf{x}$. In Eq. 4, μ is the kinematic viscosity; $c_{v,w}$ and $c_{v,a}$ are specific heat capacities of water and air, respectively; α_t is thermal eddy diffusivity and K represents the specific kinetic energy, which is calculated from $K = 0.5 |\mathbf{U}|^2$.

In Eq. 3, σ is the surface tension. Regarding the significance of the surface tension term, it is noted that in the current study, Eötvös number (the ratio of buoyancy and interfacial tension forces i.e., $\rho_w g D^2 / \sigma$) and Morton numbers (the ratio of viscous and interfacial tension forces i.e., $g \mu_w^4 / [\rho_w \sigma^3]$), are 3106 and 4.5×10^{-13} , respectively. Therefore, surface tension is expected to be negligible in the simulations. Considering the complexity of the flow, however, the validity of this statement was tested by comparing the results of two simulations with identical configuration except for the surface tension; one case with a value of zero and another case with a value of 0.073 N m^{-1} (for the pure water-air interface at 20°C). The results showed that the absence of surface tension increased the error in geyser height prediction by about 3% and pressure fluctuations were slightly stronger which shows the negligible influence of surface tension as expected.

Additionally, for tracking the air-water interface CIF solves a transport equation for volume fraction, given by:

$$\frac{\partial \alpha}{\partial t} + \mathbf{U} \cdot \nabla \alpha + \nabla \cdot \mathbf{U}_c \alpha (1 - \alpha) = - \frac{\alpha}{\rho_w} \frac{D \rho_w}{Dt}, \quad (5)$$

where D is the material derivative, the third term on the left-hand side is called anti-diffusion and \mathbf{U}_c is the compression velocity. The compression velocity is an artificial diffusion term introduced into the equation for decreasing the smearing of the free surface (Jasak, 1996; Rusche, 2002; Ubbink, 1997).

Regarding turbulence modeling, Chegini and Leon (2018) showed that realizable $k-\varepsilon$ is the most suitable model for simulating geyser events in vertical shafts. Therefore, this model is used for all the simulations performed in the current study. It is noted that realizable $k-\varepsilon$ model is implemented in OpenFOAM based on Shih et al. (1995).

Moreover, the discretization of the governing equations in OpenFOAM is based on a finite volume approach on collocated grid layout, i.e. all variables are located on the same grid point (Meier et al., 1999). Solution algorithm of CIF is based on a predictor-corrector method called pressure implicit split operator (PISO) (Issa, 1986; Márquez Damián, 2013). The PISO algorithm allows full coupling of velocity and pressure in each time-step which is necessary for transient simulations.

In the current study, a second order scheme with a flux limiter (van Leer, 1997) was considered for the spatial discretization and a second-order scheme for the temporal discretization called Crank-Nicolson. Additionally, the maximum Courant number was set to 0.5.

3 Results and Discussion

The validity of CIF for simulating geyser events was verified using the experimental data in Leon et al. (2018). A schematic of this experimental setup is shown in Fig. 1 where h_d is the length of the vertical shaft, L_u and L_d are lengths of the horizontal pipe at the upstream and downstream sides of the vertical shaft, respectively. The horizontal pipe and the vertical shaft both have the same diameter, D_d , and V_a denotes the volume of the air tank. The values of these parameters are given in Table 1. It is noted that four different vertical shaft lengths, h_d , were used in the experiments, one of which ($h_d = 6.096 \text{ m}$) was selected for the current study.

The obtained numerical results in this study are compared based on six criteria, three of which are used for validating the model based on the experimental data. The remaining three provide a basis for further analysis of the obtained numerical results. These criteria are as follows:

- (1) Pressure fluctuations: Leon et al. (2018) reported pressure data from nine pressure transducers, two of which were considered for comparing with numerical results; P1 on the top of the tank, which represents fluctuations of air pressure, and P4 at the bottom of the vertical shaft. The coordinates of these two sensors are given in Table 1. Moreover, Leon et al. (2018) repeated the experiments for each case 29 times, two of which were selected for validating the numerical model.
- (2) Geyser height, h_g , and its corresponding error, E_h : Geyser height in Leon et al. (2018) is reported as the maximum height that the eruptions attain, measured from the top of the vertical shaft. Therefore, for consistency, geyser height in this study is obtained by subtracting the height of the vertical shaft (6.096 m) from the highest y -coordinate among the cells in the atmospheric domain that have a volume fraction of at least 0.5. The corresponding error is determined with respect to the average geyser height obtained in the experiments for the 6 m vertical shaft. The average geyser height for the 6 m vertical shaft was 12.25 m and the error was ± 0.87 m.
- (3) Snapshots of flow patterns: During the experiments, different flow patterns were observed and captured using a high-speed camera. The camera footage was used for a qualitative comparison of the flow patterns in the horizontal pipe and the vertical shaft with those of the simulations.
- (4) Peak time, t_p : The time at which the most intense eruption occurs. This parameter provides a quantitative measure of the time required for the most intense eruption to form in each simulation.
- (5) Velocity fluctuations at the exit of the vertical shaft, U , and the maximum exit velocity, U_{max} : At each time step, this velocity was obtained by calculating the weighted average of cells velocity that are located at the top of the vertical shaft using

$$U = \frac{\sum \alpha_i V_i U_i}{\sum \alpha_i V_i}$$

where V_i , α_i and U_i denote volume, water volume fraction and velocity magnitude of a cell respectively. This parameter provides a qualitative measure for tracking the occurrence of eruptions.

- (6) Computation time, t_s , as a measure of the required computational effort for each simulation. It is noted that all the simulations were performed using one node with 28 cores and Intel Xeon E5-2680v4 CPUs.

It is noted that the first three criteria are comparisons with the experimental data and the remaining items are obtained only from the numerical results. Moreover, based on the simulations, one of the major differences among the simulations is the onset of the geysering. For instance, Fig. 2 shows the velocity fluctuations at the exit of the vertical shaft for three different initial pressure head differences and the following points can be discerned from the figure:

- General characteristics of geyser events, which are described in detail in Section 3.5, are almost the same in all the cases.
- Spikes in the graphs, which are indicative of the occurrence of eruptions, follow the same trend in all cases.
- Changing the parameters shifts the peak time, t_p , but the geysering occurs more or less in a period of eight seconds for all cases.

These observations hold true for all the other numerical results obtained in this study, as will be shown in the following sections. Therefore, all pressure graphs presented in this study are plotted in

a time range of eight seconds, which corresponds to the geyser duration for the conditions discussed herein.

A summary of the parameters of interest in the current study is given in Table 2. Each category is denoted by a two-letter abbreviation which is used for specifying the configuration of each simulation throughout the paper, e.g. SD=2D and PD=0.05 means that the simulation is performed in 2D and the initial pressure head difference is 0.05 m. The boldface font denotes the most efficient option in terms of accuracy and computation time for each category.

3.1 Numerical Setup

A 3D mesh of the geometry of the experimental setup in Leon et al. (2018) was generated using SALOME (Open Cascade, 2017) and snappyHexMesh, an OpenFOAM meshing utility. A snapshot of the generated mesh is presented in Fig. 3 where the whole domain is shown on the left side of the figure and two slices of the mesh are shown on the right. A cylinder is attached to the top of the vertical shaft, representing the atmospheric region for capturing eruptions and measuring geyser height. The cylinder has a diameter of 1 m. Also, given that the obtained geyser height in the experiment is about 12 m, the height of the atmospheric domain is set to 15 m so it does not affect the flow in the simulation. The mesh is structured, as it is generally more suitable for multiphase flow simulations (Bayon et al., 2016), and hexahedral dominant.

Regarding boundary conditions, the no-slip boundary condition is applied on the walls for the velocity field and zero gradient for the other fields. On the atmospheric domain, the total pressure (sum of static and dynamic pressures) is set to a fixed value of 102,032 Pa (the atmospheric pressure reported in Leon et al. (2018)) and other fields are set to zero gradient. Considering the use of the realizable k - ϵ for turbulence model, boundary layers near the walls are modeled using wall functions for turbulence parameters; turbulence kinetic energy, k and turbulence dissipation rate, ϵ .

With regards to initial conditions, several values were used for the initial pressure head difference between the air tank (point B in Fig. 1) and the bottom of the vertical shaft (point A in Fig. 1) or “initial pressure head difference” for short. Furthermore, the average initial temperatures of water and air in the experiments were reported as 19.21 °C and 18.64 °C, respectively, which are used as initial conditions for temperature fields. The validation and subsequent numerical investigations were performed based on three criteria: spatial dimensions (2D and 3D), initial pressure head difference and compressibility of phases.

A mesh convergence study was carried out to determine the most efficient mesh size in terms of accuracy and computation time. Starting from a coarse mesh with a maximum cell length, h_{max} , of 0.04 m, the mesh was refined by a factor of two to generate a new mesh. After each refinement, the obtained numerical results were compared with the experimental data. This process was repeated until the results of the refined mesh were in close agreement with the previous mesh and the experimental data. Results of the mesh convergence study are shown in Fig. 4 and Table 3 where N is the total number of cells.

As observed in Fig. 4 and Table 3, the coarse mesh produces unacceptable results while both medium and fine meshes are in good agreement with the experiments. Therefore, considering the noticeable decrease in computational time from the fine mesh to the medium and the negligible differences in their performance, a maximum cell length of 0.02 m (the medium mesh) was used for the rest of the simulations.

Additionally, for 2D simulations, a 2D mesh (x and y directions in Fig. 1) of the geometry was generated using another OpenFOAM utility, blockMesh, with similar refinements as the 3D mesh and maximum cell length of 0.02 m per the mesh convergence study.

3.2 *Spatial Dimensions*

Even though geyser flows are thought to be highly three-dimensional, to investigate whether geysers could be represented with good accuracy in 2D, two simulations were carried out in 2D and 3D under similar numerical conditions and compared with the experiments in [Leon et al. \(2018\)](#). A qualitative comparison of numerical and experimental results is shown in Figs 5 and 6 which illustrates the flow patterns formed in the horizontal pipe and the vertical shaft during the formation of the geyser. Additionally, a quantitative comparison is provided in Fig. 7 and Table 4.

These results show that the 2D model captures reasonably well the flow pattern transitions that occur during the formation of geysers. Moreover, the comparison of pressure traces and geyser height shows that both 2D and 3D simulations are in good agreement with the experimental data. This is an exciting and promising finding since the length scales of stormsewer systems is typically in the order of thousands of meters so the use of a 3D model for simulating geyser events is computationally very expensive and not practical. A 2D model, if established to be accurate for simulating geysers, could be an effective and a practical tool, especially for qualitative studies. It is clear that actual stormsewer systems are more complex than the experimental setup in [Leon et al. \(2018\)](#) in terms of geometry and boundary conditions and thus, further studies are needed before the 2D model is recommended for simulating geysering events.

3.3 *Initial pressure head difference*

In the experimental tests in [Leon et al. \(2018\)](#), right before air entered the horizontal pipe, the water and air were quiescent and in an apparent equilibrium. According to the pressure head traces in [Leon et al. \(2018\)](#), right before the air entered the horizontal pipe, the pressure difference between the air tank (P1) and the bottom of the vertical shaft (P4) was almost zero for all the experimental runs. In the numerical simulations, a “small” pressure head difference is required to push the air into the horizontal pipe. In order to determine this “small” required initial pressure head difference for accurate simulation of the experiments, a sensitivity analysis was performed. Five simulations were carried out with five different pressure head differences, three of which are reported here for brevity and clarity; 0.01 m, 0.05 m and 0.10 m. It is noted that an initial pressure head difference of 0.1 m gives a pressure head slope of 1.6 % ($0.1/6.274$) for the present geometry. The results are presented in Fig. 8 and Table 5.

The three reported cases are in good agreement with the results of the experiments. According to the velocity traces in Fig. 8, and as expected, geysering occurs earlier when the initial pressure head difference is increased. Also, the reported geyser height in Table 5 and pressure traces in Fig. 8 show that the geyser characteristics are similar when the initial pressure head difference is below 0.1 m (1.6 % pressure head slope). However, for larger initial pressure head differences, which are not reported in this paper, the pressure traces and geyser height predictions deviate significantly from the experiments. Moreover, an initial pressure head difference of 0.1 m, sped up the simulation by about 30 % compared to a pressure head difference of 0.01 m. It is noted that this threshold is obtained for the specified geometry and boundary conditions, and might be different for other conditions. Moreover, considering that the results with a 0.05 m initial pressure head difference are in better agreement with the experimental data compared to the 0.1 m case and given that the computation time difference between these two cases is not substantial, the 0.05 m initial pressure difference (0.8 % pressure head slope) is deemed as the efficient value.

It is noteworthy that according to Table 5, the geyser height decreases by increasing the initial pressure head difference. It is speculated that this reduction is related to the amount of remaining water in the system after the first few weak eruptions (e.g., right before the strongest eruption). While the air pocket is approaching the vertical shaft, higher initial pressure head difference increases the initial spillage of water from the top of the vertical shaft (see Section 3.5 for details). Therefore, after the first few weak eruptions and right before the strongest eruption, the remaining water in

the system is smaller than the cases with lower initial pressure head differences. As a result, for the conditions of the presented study, increasing the initial pressure head difference decreases the geyser height. This decrease, however, might not take place in actual stormsewer systems as they typically have a large supply of water.

3.4 Compressibility

Generally, for single phase flows compressibility could be neglected in numerical simulations based on Mach number while in multiphase flows such assumption should be investigated. In the case of geysering, the dynamics of air pockets in the horizontal pipe and the vertical shaft plays a key role in the formation of geysers (Leon, 2018). Moreover, rapid changes in pressure and velocity fields during the geysering may lead to sudden and significant expansions and contractions of the air phase. To study the importance of compressibility of the phases in geysering four scenarios were considered; both phases as incompressible/compressible and only one phase as incompressible.

The obtained results indicate that when both phases were considered incompressible, the model was unable to produce a geyser. The same holds true for the case where only air was considered incompressible. By setting only water as incompressible, however, the model successfully produced geysers which demonstrates the importance of compressibility of air. Obviously, the case where both phases were compressible was also able to simulate geysering. Figure 9 and Table 6 compares the results of these two successful cases with the experimental data.

As observed, both successful cases [(1) water and air are compressible, (2) air is compressible and water is incompressible] are in good agreement with the experimental data, although the incompressible water case presents slightly stronger fluctuations. This is not surprising as very rapid flow changes (e.g., geyser flows) are not well represented by models that neglect water compressibility and those models are often overly conservative of pressure changes (e.g., Jung and Karney (2016)). Considering that the computational effort for both successful cases are almost the same while the case where air and water are considered compressible is more accurate, this case was deemed as the most efficient option.

3.5 Geyser Mechanisms

Based on the presented results, following we briefly describe the mechanisms preceding and during geyser eruptions for the experimental setup in Leon et al. (2018). These mechanisms may differ for other geometry configurations and other initial and boundary conditions. The mechanisms for the setup used are in agreement with the mechanisms described in Leon (2018) and are as follows

- (1) A large air pocket is admitted to the horizontal pipe from the bottom of the air tank. It progresses toward the vertical shaft as shown in Fig. 9(a). Up to about 15 s after beginning of the simulation (Fig. 9(b)) the flow regime in the horizontal pipe is stratified/wavy.
- (2) As can be observed in Figs 10(a)–10(c), water spills at the top of the vertical shaft while a few Taylor-like bubbles ascend in the vertical pipe.

The aforementioned water spillage at the top of the vertical pipe translates into a decrease in the hydrostatic pressure in the vertical shaft. This pressure decrease results in a rapid velocity increase of the air flow in the horizontal and vertical pipe. The high velocity in the horizontal pipe leads to instabilities (e.g., Kelvin–Helmholtz instability), which in turn leads to a change in the flow regime to slug flow, which is a series of liquid plugs (slugs) separated by relatively large air compartments. The slugs have initially the same pressure and they create a discontinuity that blocks the uniform release of air from the horizontal pipe to the vertical shaft. At this time, the flow in the vertical shaft is highly mixed and turbulent. Once the slugs are formed in the horizontal pipe, they are violently propelled through the vertical shaft right after a sudden drop of pressure in the vertical shaft (e.g., after the previous eruption). The

propelling of each liquid slug is activated whenever a significant pressure gradient between the slug and the vertical shaft is attained. The discontinuity produced by the slugs allow to maintain the pressure inside the slugs and hence allows to still achieve significant pressure gradients (between the slug and vertical shaft) after the first geyser eruption. These results are written with the help of Figs 10–12.

- (3) After occurrence of the most intense eruption, there may be a few more eruptions, however as water is depleted, the horizontal pipe is depressurized, which is followed by the termination of the geysering process (Fig. 9(f)).

4 Conclusion

The present study investigated characteristics of geysers in a vertical shaft using numerical simulations carried out in OpenFOAM. The model was validated using experimental data in Leon et al. (2018) based on pressure traces, geyser height and snapshots of the flow in the system. Although geysering is often considered an intrinsically 3D phenomenon, the geyser experiments in Leon et al. (2018) was modeled in 2D with good accuracy. Further work is needed to verify the applicability of 2D models for simulating geysers in actual stormsewer systems. Furthermore, the influence of compressibility of water and air in the simulation of geyser events was studied. The results show that air compressibility is crucial for simulating geysers events, while water compressibility is not. The study also discussed the flow patterns during a geysering event as well as the mechanisms preceding and during the geyser eruptions. As a subsequent study, the validated model will be used to explore solutions for preventing the occurrence of geysers in stormsewer systems.

Acknowledgments

The authors would like to thank the three anonymous reviewers for their constructive comments that improved the quality of this study. The first author also would like to thank Dr. Rodolfo Ostilla Mónico for providing insightful suggestion. We acknowledge the support from the Center for Advanced Computing and Data Science at the University of Houston for the use of the Sabine Cluster.

Funding

The authors gratefully acknowledge the financial support of the U.S. Environmental Protection Agency under Grant number R8335187. This manuscript has not been formally reviewed by EPA. The views expressed are solely those of the authors. EPA does not endorse any products or commercial services mentioned.

Notations

| | | |
|----------------|---|--|
| $c_{v,w}$ | = | Specific heat capacity of water ($\text{J kg}^{-1} \text{K}^{-1}$) |
| $c_{v,a}$ | = | Specific heat capacity of air ($\text{J kg}^{-1} \text{K}^{-1}$) |
| D_d | = | Diameter of all pipes (m) |
| E_h | = | Error in computation of the geyser height (-) |
| g | = | Gravitational acceleration (m s^{-2}) |
| h_d | = | Length of vertical shaft (m) |
| h_g | = | Geyser height (m) |
| h_{max} | = | Maximum cell length in a mesh (m) |
| L_d | = | Length of horizontal pipe at the downstream side of the vertical shaft (m) |
| L_u | = | Length of horizontal pipe at the upstream side of the vertical shaft (m) |
| K | = | Specific kinetic energy ($\text{m}^2 \text{s}^{-2}$) |
| k | = | Turbulence kinetic energy (J kg^{-1}) |
| N | = | Number of cells in a mesh (-) |
| p | = | Pressure field (Pa) |
| R_w | = | Vapor constant ($\text{J kg}^{-1} \text{K}^{-1}$) |
| R_a | = | Gas constant ($\text{J kg}^{-1} \text{K}^{-1}$) |
| t_p | = | Time shift of pressure graph (s) |
| t_s | = | Computation time of simulation (min) |
| T | = | Temperature field (K) |
| \mathbf{U} | = | Velocity field (m s^{-1}) |
| \mathbf{U}_c | = | Compression velocity (m s^{-1}) |
| U | = | Magnitude of the exit velocity (m s^{-1}) |
| U_{max} | = | Magnitude of the maximum exit velocity (m s^{-1}) |
| V | = | Volume of a cell (m^3) |
| V_a | = | Volume of the air tank (m^3) |
| \mathbf{x} | = | Position vector (m) |
| α | = | Volume fraction of water phase (-) |
| α_t | = | Thermal eddy diffusivity ($\text{kg m}^{-1} \text{s}^{-1}$) |
| ε | = | Turbulence dissipation rate ($\text{J kg}^{-1} \text{s}^{-1}$) |
| κ | = | Curvature of interface (-) |
| μ | = | Kinematic viscosity ($\text{m}^2 \text{s}^{-1}$) |
| ρ_0 | = | Initial density of water (kg m^{-3}) |
| ρ_a | = | Density of air (kg m^{-3}) |
| ρ_w | = | Density of water (kg m^{-3}) |
| σ | = | Surface tension (N m^{-1}) |

References

- Bayon, A., Valero, D., Garcia-Bartual, R., Valles-Moran, F. J., and Lopez-Jimenez, P. A. (2016). Performance assessment of OpenFOAM and FLOW-3d in the numerical modeling of a low reynolds number hydraulic jump. *Environmental Modelling & Software*, 80:322–335.
- CD-adapco (2012). *Star-CCM+ 7*. CD-adapco Inc., Melville, NY, USA.
- CFD Direct (2017). *OpenFOAM 5.0*. The OpenFOAM Foundation Ltd, London, United Kingdom.
- Chan, S. N., Cong, J., and Lee, J. H. W. (2018). 3d numerical modeling of geyser formation by release of entrapped air from horizontal pipe into vertical shaft. *Journal of Hydraulic Engineering*, 144(3):04017071.
- Chegini, T. and Leon, A. S. (2018). Comparison of various turbulence models for violent geysers in vertical pipes. In *World Environmental and Water Resources Congress 2018*. American Society of

- Civil Engineers.
- Choi, Y. J., Leon, A. S., and Apte, S. V. (2014). Three-dimensional numerical modeling of air-water geyser flows. In *World Environmental and Water Resources Congress 2014*. American Society of Civil Engineers.
- Cong, J., Chan, S. N., and Lee, J. H. W. (2017). Geyser formation by release of entrapped air from horizontal pipe into vertical shaft. *Journal of Hydraulic Engineering*, 143(9):04017039.
- Guo, Q. and Song, C. C. S. (1991). Dropshaft hydrodynamics under transient conditions. *Journal of Hydraulic Engineering*, 117(8):1042–1055.
- Hamam, M. A. and McCorquodale, J. A. (1982). Transient conditions in the transition from gravity to surcharged sewer flow. *Canadian Journal of Civil Engineering*, 9(2):189–196.
- Issa, R. (1986). Solution of the implicitly discretised fluid flow equations by operator-splitting. *Journal of Computational Physics*, 62(1):40–65.
- Jasak, H. (1996). *Error Analysis and Estimation for the Finite Volume Method with Applications to Fluid Flows*. PhD thesis, Imperial College of Science, Technology and Medicine.
- Jung, B. S. and Karney, B. (2016). A practical overview of unsteady pipe flow modeling: from physics to numerical solutions. *Urban Water Journal*, 14(5):502–508.
- Leon, A. S. (2018). Mechanisms that lead to violent geysers in vertical shafts. *Journal of Hydraulic Research*, pages 1–12.
- Leon, A. S., Elayeb, I., and Tang, Y. (2018). An experimental study on violent geysers in vertical pipes. *Journal of Hydraulic Research (accepted)*.
- Lewis, J. W. (2011). *A Physical Investigation of Air/Water Interactions Leading to Geyser Events in Rapid Filling Pipelines*. PhD thesis, University of Michigan.
- Ma, Z., Causon, D., Qian, L., Mingham, C., and Ferrer, P. M. (2016). Numerical investigation of air enclosed wave impacts in a depressurised tank. *Ocean Engineering*, 123:15–27.
- Márquez Damián, S. (2013). *An extended mixture model for the simultaneous treatment of short and long scale interfaces*. PhD thesis, Universidad Nacional del Litoral, Argentina.
- Meier, H., Alves, J., and Mori, M. (1999). Comparison between staggered and collocated grids in the finite-volume method performance for single and multi-phase flows. *Computers & Chemical Engineering*, 23(3):247–262.
- MN Dot (1999). 7/3/1999 full raw traffic camera catching explosive storm sewer flooding - full video. Technical report, Youtube.
- Muller, K. Z., Wang, J., and Vasconcelos, J. G. (2017). Water displacement in shafts and geysering created by uncontrolled air pocket releases. *Journal of Hydraulic Engineering*, 143(10):04017043.
- Open Cascade (2017). *SALOME 8.2*. Open Cascade Inc., Guyancourt, France.
- Rusche, H. (2002). *Computational Fluid Dynamics of Dispersed Two-Phase Flows at High Phase Fractions*. PhD thesis, University of London.
- Shih, T.-H., Liou, W. W., Shabbir, A., Yang, Z., and Zhu, J. (1995). A new $k-\epsilon$ eddy viscosity model for high reynolds number turbulent flows. *Computers & Fluids*, 24(3):227–238.
- Ubbink, O. (1997). *Numerical prediction of two fluid systems with sharp interfaces*. PhD thesis, University of London PhD Thesis.
- van Leer, B. (1997). Towards the ultimate conservative difference scheme. *J. Comput. Phys.*, 135(2):229–248.
- Vasconcelos, J. G. and Wright, S. J. (2005). Experimental investigation of surges in a stormwater storage tunnel. *Journal of Hydraulic Engineering*, 131(10):853–861.
- Vasconcelos, J. G. and Wright, S. J. (2011). Geysering generated by large air pockets released through water-filled ventilation shafts. *Journal of Hydraulic Engineering*, 137(5):543–555.
- Vasconcelos, J. G., Wright, S. J., and Roe, P. L. (2009). Numerical oscillations in pipe-filling bore predictions by shock-capturing models. *Journal of Hydraulic Engineering*, 135(4):296–305.
- Wright, S. J., Lewis, J. W., and Vasconcelos, J. G. (2011). Geysering in rapidly filling storm-water tunnels. *Journal of Hydraulic Engineering*, 137(1):112 – 115.
- Yen, B. C., Pansic, N., et al. (1980). Surge of sewer systems. Technical report, University of

Illinois at Urbana-Champaign. Water Resources Center.

List of Tables

| | | |
|---|---|----|
| 1 | Geometry parameters of the experimental setup in Leon et al. (2018) | 14 |
| 2 | Categories of simulations parameters | 15 |
| 3 | Summary of the mesh convergence study with three mesh refinement levels | 16 |
| 4 | Comparison of 2D and 3D simulations | 17 |
| 5 | Comparison of simulations with different initial pressure head differences | 18 |
| 6 | Comparison of simulations with water phase being considered incompressible and compressible | 19 |

Table 1 Geometry parameters of the experimental setup in Leon et al. (2018)

| Parameters | Value |
|------------------------------------|---------------------|
| Volume of tank (V_a) | 1.7 m ³ |
| Diameter of pipes (D_d) | 0.152 m |
| Horizontal pipe length* (L_u) | 6.274 m |
| Horizontal pipe length** (L_d) | 3.073 m |
| vertical shaft length (h_d) | 6.096 m |
| P1 sensor coordinate | (9.347, 1.000, 0) m |
| P4 sensor coordinate | (3.149, 0.812, 0) m |

* upstream of the vertical shaft

** downstream of the vertical shaft

Table 2 Categories of simulations parameters

| (SD) Spatial Dimensions | (PD) Pressure Head Difference (m) | (CW) Compressibility of Water |
|----------------------------|--------------------------------------|----------------------------------|
| 2D | 0.00 | Compressible |
| 3D | 0.05 | Incompressible |
| | 0.10 | |

Boldface font indicates the computationally efficient option

Table 3 Summary of the mesh convergence study with three mesh refinement levels

| Level | N | h_{max} (m) | U_{max} (m s ⁻¹) | h_g (m) | $E(\%)$ | t_p (s) | t_s (min) |
|--------|------------|---------------|--------------------------------|-----------|---------|-----------|-------------|
| Fine | 16,531,313 | 0.01 | 34.98 | 12.98 | 5.9 | 17.56 | 39,564 |
| Medium | 2,088,410 | 0.02 | 34.12 | 11.62 | 5.1 | 22.30 | 4725 |
| Coarse | 270,555 | 0.04 | 33.34 | 8.94 | 27.0 | 49.34 | 1456 |

SD=3D, PD=0.05, CW=compressible

Table 4 Comparison of 2D and 3D simulations

| SD | U_{max} (m s ⁻¹) | h_g (m) | $E(\%)$ | t_p (s) | t_s (min) |
|----|--------------------------------|-----------|---------|-----------|-------------|
| 2D | 32.62 | 11.31 | 7.7 | 25.83 | 63 |
| 3D | 34.12 | 11.62 | 5.1 | 22.30 | 4725 |

PD=0.05, CW=compressible

Table 5 Comparison of simulations with different initial pressure head differences

| PD | U_{max} (m s ⁻¹) | h_g (m) | $E(\%)$ | t_p (s) | t_s (min) |
|--------|--------------------------------|-----------|---------|-----------|-------------|
| 0.01 m | 34.41 | 12.08 | 1.39 | 61.04 | 89 |
| 0.05 m | 32.62 | 11.31 | 7.7 | 25.83 | 63 |
| 0.10 m | 37.84 | 8.62 | 29.6 | 14.50 | 61 |

SD=2D, CW=compressible

Table 6 Comparison of simulations with water phase being considered incompressible and compressible

| CW | U_{max} (m s ⁻¹) | h_g (m) | E (%) | t_p (s) | t_s (min) |
|----------------|--------------------------------|-----------|---------|-----------|-------------|
| Compressible | 32.62 | 11.31 | 7.7 | 25.83 | 63 |
| Incompressible | 33.11 | 11.46 | 6.4 | 24.61 | 62 |

SD=2D, PD=0.05

List of Figures

1 A schematic of the experimental setup in Leon et al. (2018) 21

2 Comparison of velocity fluctuations at the exit of the vertical shaft (U) with different initial pressure head differences (SD=2D, CW=compressible) 22

3 3D mesh of the experimental setup in Leon et al. (2018) with medium refinement 23

4 Results of simulations for the mesh convergence study at pressure probes (a) P1 and (b) P4 and (c) velocity fluctuations at the exit of the vertical shaft (SD=3D, PD=0.05, CW=compressible) 24

5 Snapshots of the simulation (colorful images) and the experiment (grayscale images) in the horizontal pipe at (a) $t = 115.3$ s (Stratified/wavy flow), (b) $t = 118.2$ s (Slug flow) and (c) $t = 118.6$ s; the air-water interface in the experiment's snapshots are highlighted with red (SD=2D, PD=0.05, CW=compressible) 25

6 Snapshots of the simulation (colorful images) and the experiment in Leon et al. (2018) (grayscale images) through the vertical shaft at (a) $t = 114.4$ s (Slug flow), (b) 120.5 s (Churn flow) and (c) 123.2 s (Annular flow); the air-water interface in the experiment's snapshots are highlighted with red (SD=2D, PD=0.05, CW=compressible) 26

7 Results of 2D and 3D simulations at pressure probes (a) P1 and (b) P4 and (c) velocity fluctuations at the exit of the vertical shaft (PD=0.05, CW=compressible) 27

8 Results of simulations for different initial pressure head difference at pressure probes (a) P1 and (b) P4 and (c) velocity fluctuations at the exit of the vertical shaft (SD=2D, CW=compressible) 28

9 Results of simulations with water phase being considered incompressible and compressible at pressure probes (a) P1 and (b) P4 and (c) velocity fluctuations at the exit of the vertical shaft (SD=2D, PD=0.05) 29

10 Snapshots of the simulation in the horizontal pipe at (a) $t = 8.0$ s (b) $t = 15.0$ s (c) $t = 18.6$ s (d) $t = 20.0$ s (e) $t = 22.0$ s (f) $t = 32.0$ s (SD=2D, PD=0.05, CW=compressible) 30

11 Snapshots of the simulation in the vertical shaft at (a) $t = 18.0$ s (b) $t = 20.0$ s (c) $t = 20.8$ s (d) $t = 21.4$ s (e) $t = 22.0$ s (SD=2D, PD=0.05, CW=compressible) 31

12 Snapshots of the simulation in the atmospheric domain at (a) $t = 19.6$ s (b) $t = 21.0$ s (c) $t = 21.6$ s (d) $t = 22.9$ s (e) $t = 23.4$ s (SD=2D, PD=0.05, CW=compressible) . . . 32

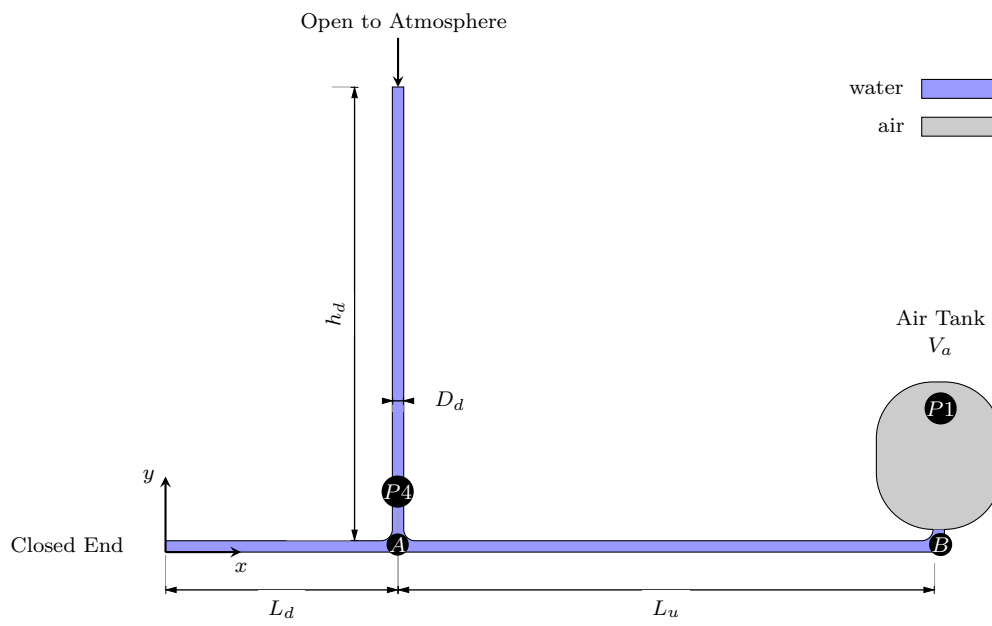


Figure 1 A schematic of the experimental setup in Leon et al. (2018)

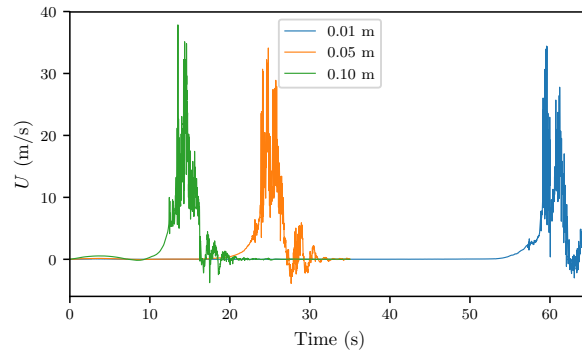


Figure 2 Comparison of velocity fluctuations at the exit of the vertical shaft (U) with different initial pressure head differences (SD=2D, CW=compressible)

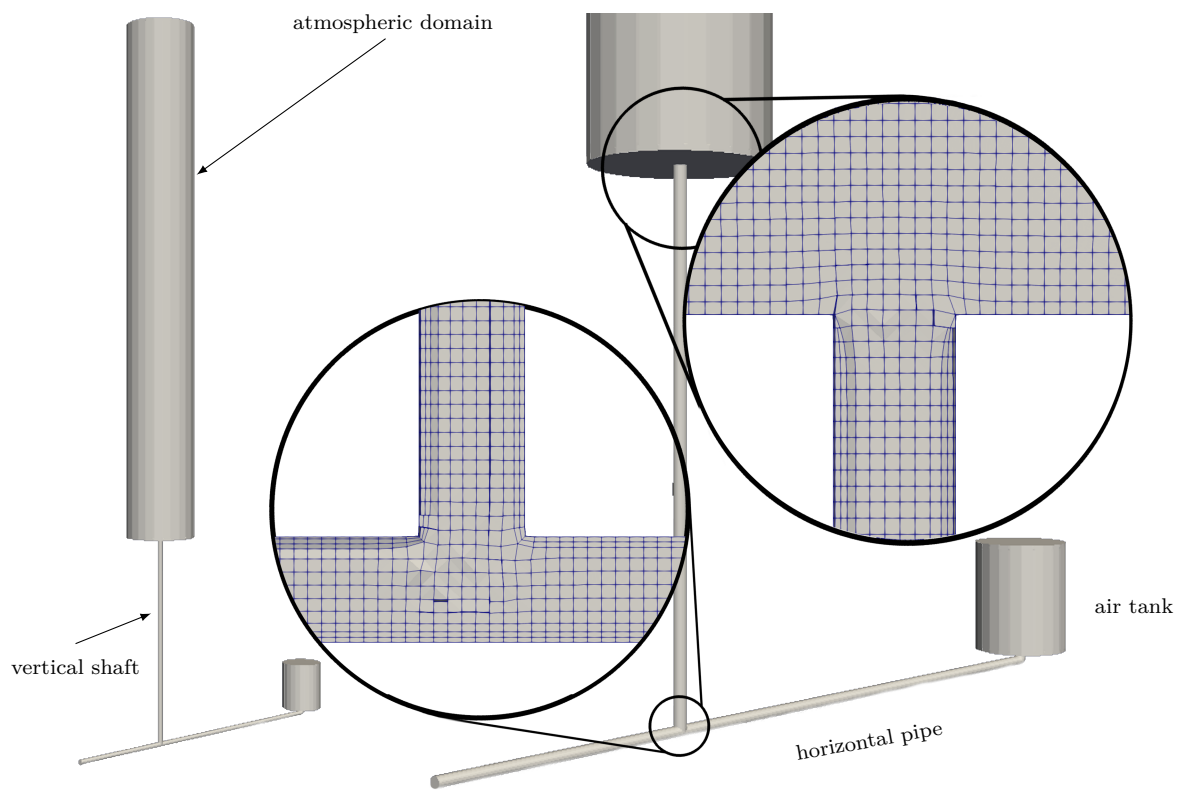


Figure 3 3D mesh of the experimental setup in Leon et al. (2018) with medium refinement

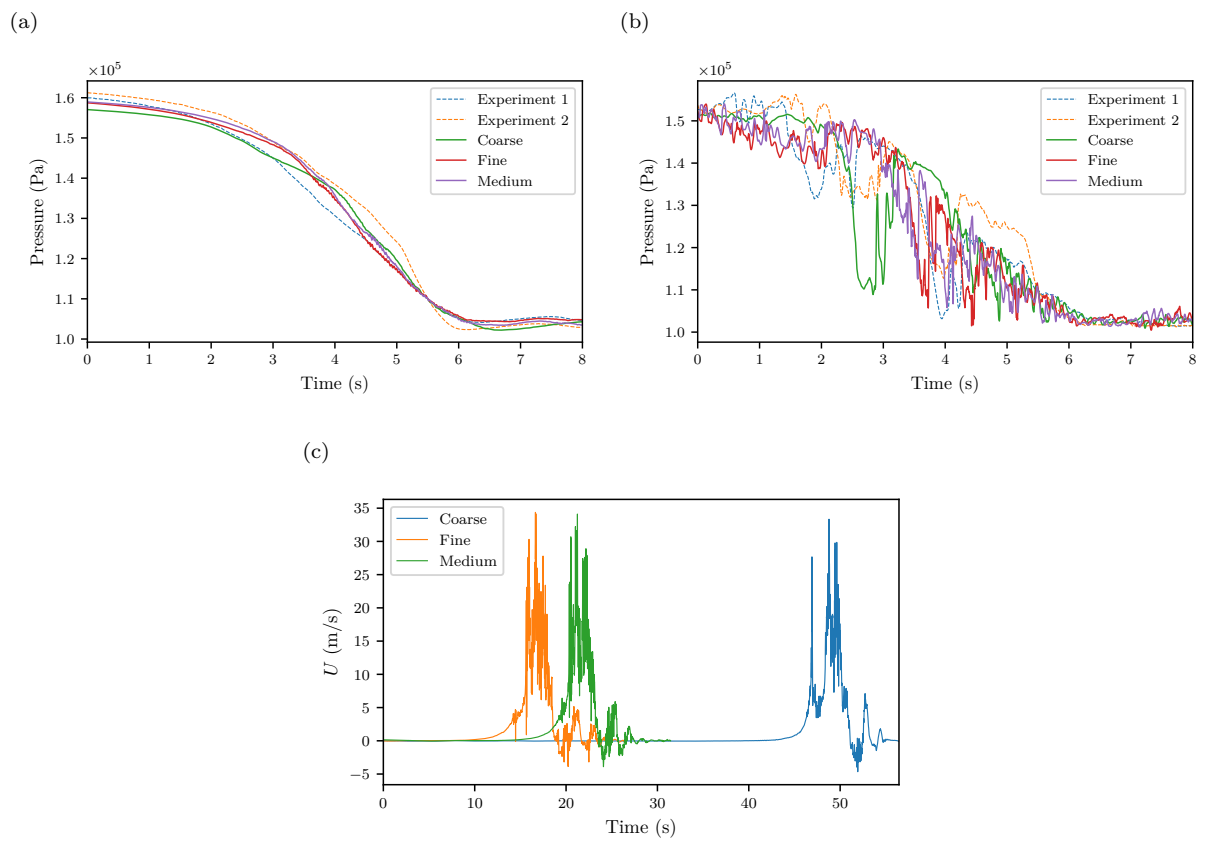


Figure 4 Results of simulations for the mesh convergence study at pressure probes (a) P1 and (b) P4 and (c) velocity fluctuations at the exit of the vertical shaft (SD=3D, PD=0.05, CW=compressible)

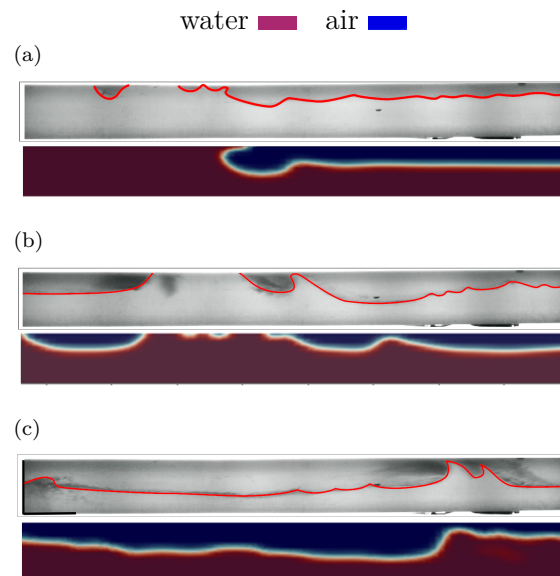


Figure 5 Snapshots of the simulation (colorful images) and the experiment (grayscale images) in the horizontal pipe at (a) $t = 115.3$ s (Stratified/wavy flow), (b) $t = 118.2$ s (Slug flow) and (c) $t = 118.6$ s; the air-water interface in the experiment's snapshots are highlighted with red (SD=2D, PD=0.05, CW=compressible)

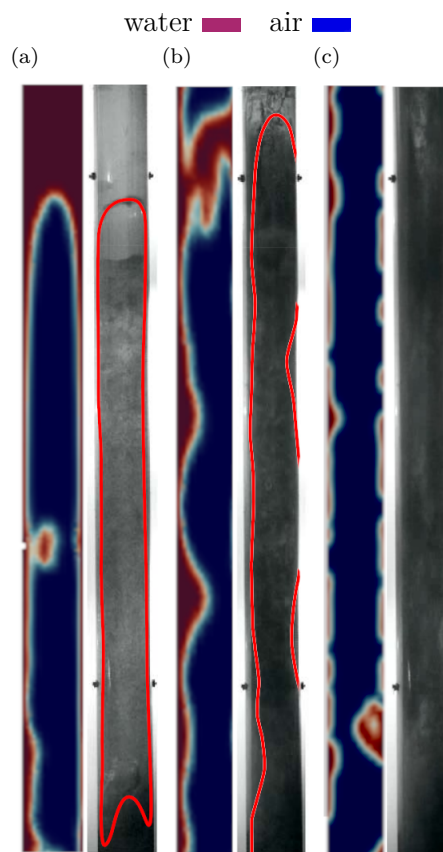


Figure 6 Snapshots of the simulation (colorful images) and the experiment in Leon et al. (2018) (grayscale images) through the vertical shaft at (a) $t = 114.4$ s (Slug flow), (b) 120.5 s (Churn flow) and (c) 123.2 s (Annular flow); the air-water interface in the experiment's snapshots are highlighted with red (SD=2D, PD=0.05, CW=compressible)

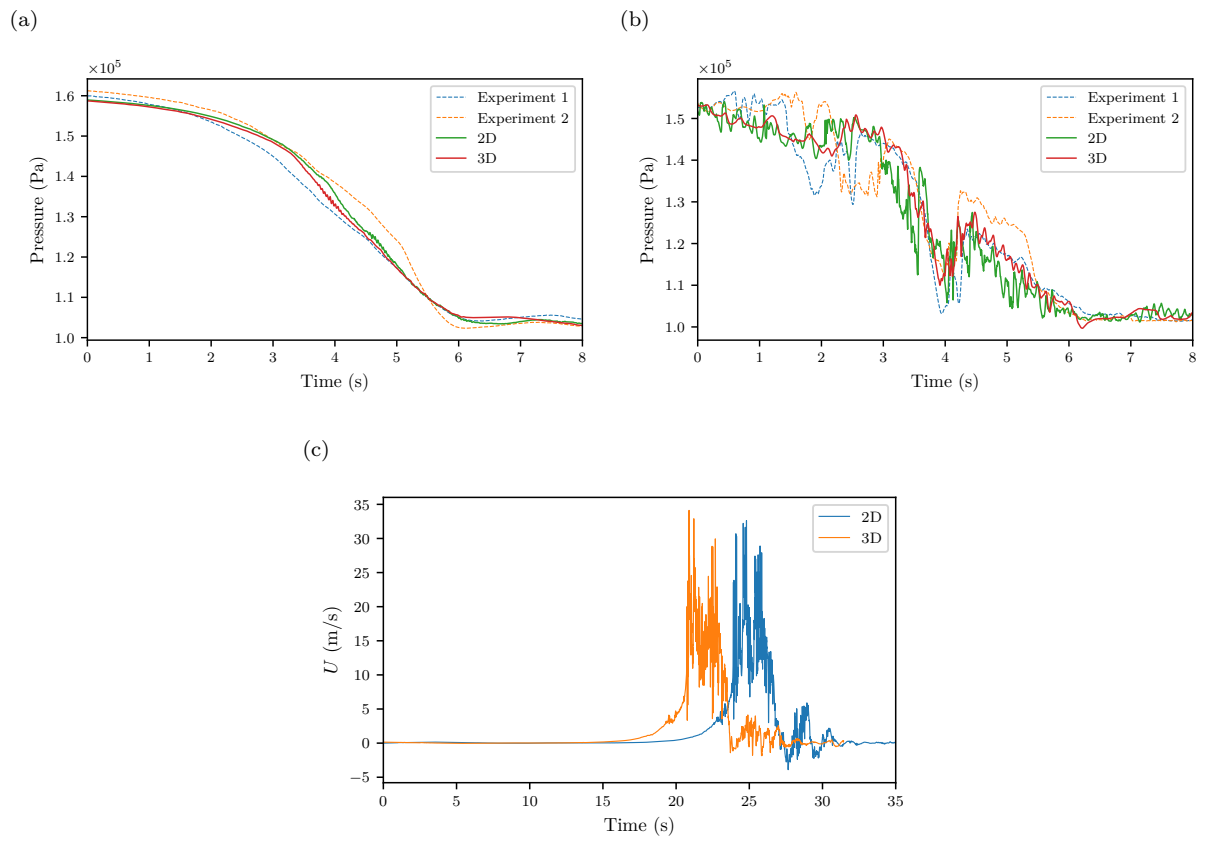


Figure 7 Results of 2D and 3D simulations at pressure probes (a) P1 and (b) P4 and (c) velocity fluctuations at the exit of the vertical shaft (PD=0.05, CW=compressible)

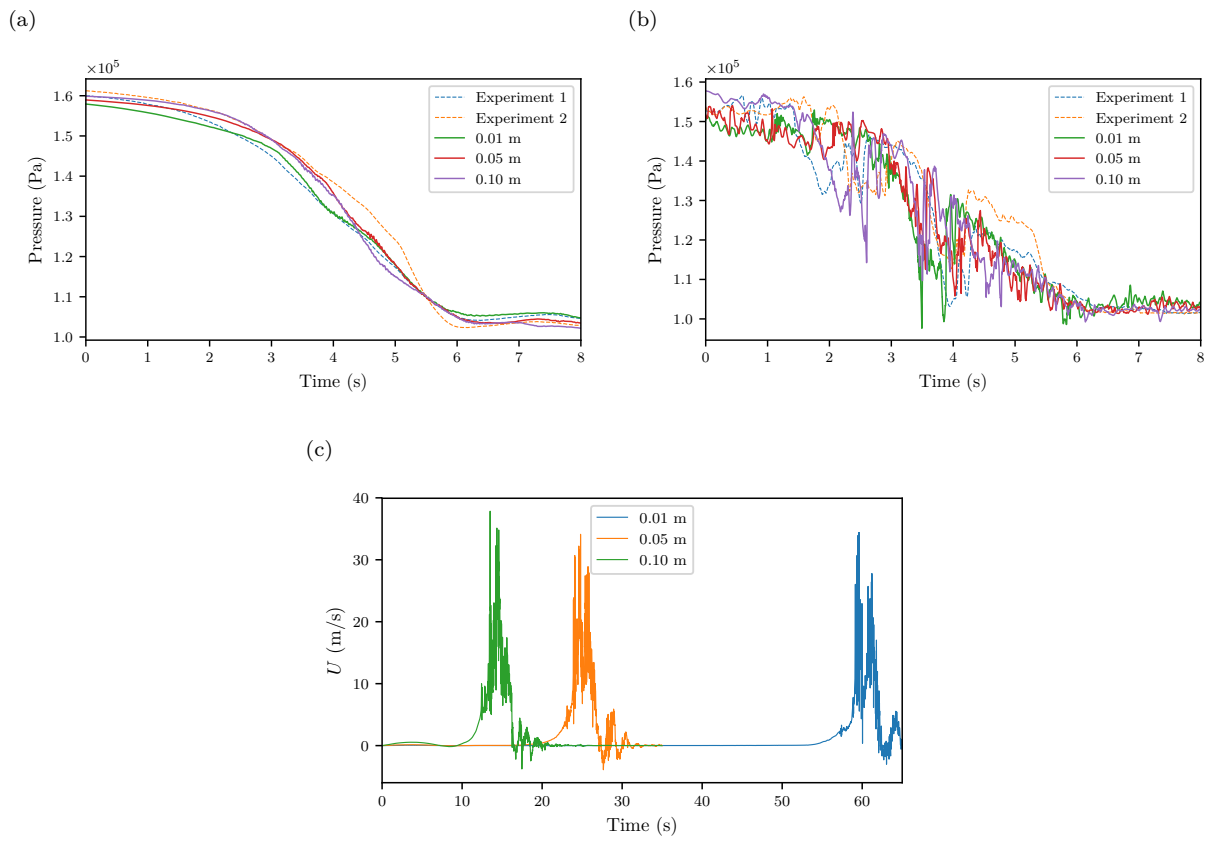


Figure 8 Results of simulations for different initial pressure head difference at pressure probes (a) P1 and (b) P4 and (c) velocity fluctuations at the exit of the vertical shaft (SD=2D, CW=compressible)

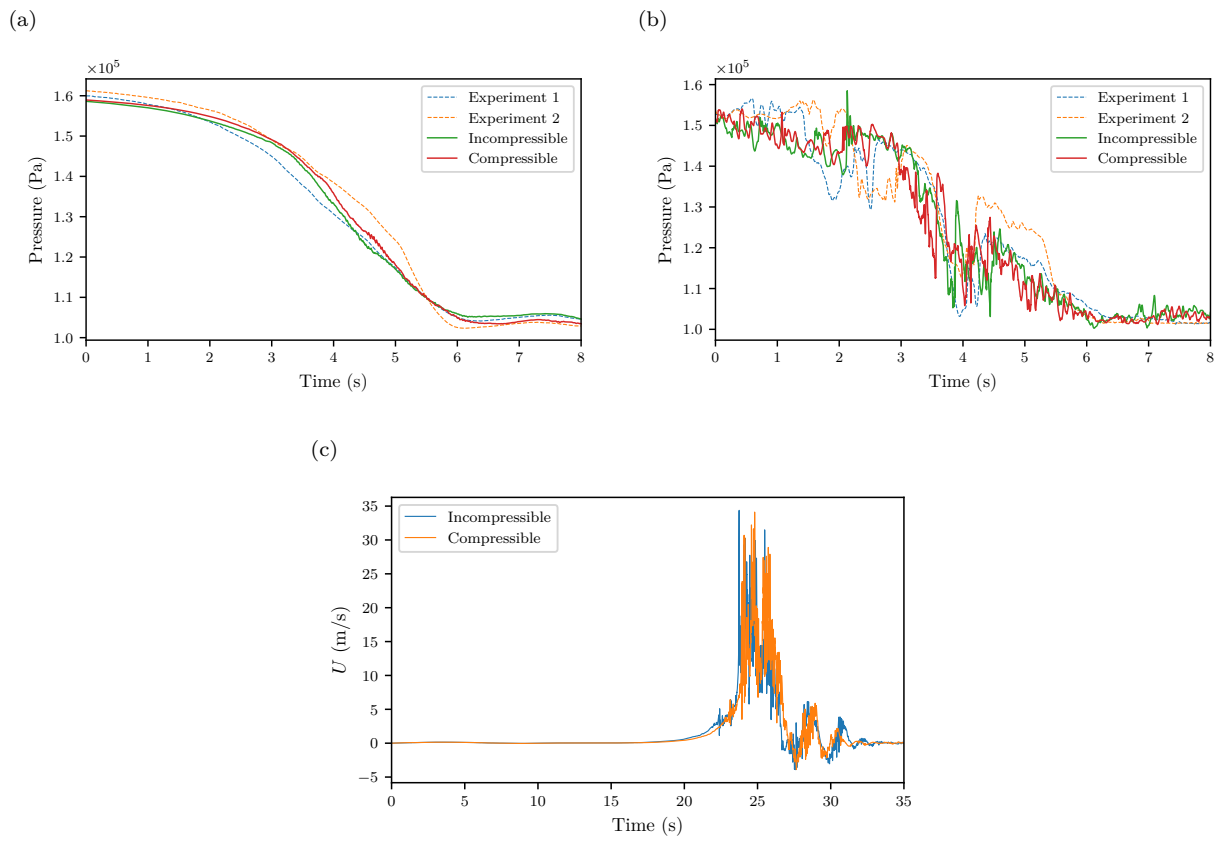


Figure 9 Results of simulations with water phase being considered incompressible and compressible at pressure probes (a) P1 and (b) P4 and (c) velocity fluctuations at the exit of the vertical shaft (SD=2D, PD=0.05)

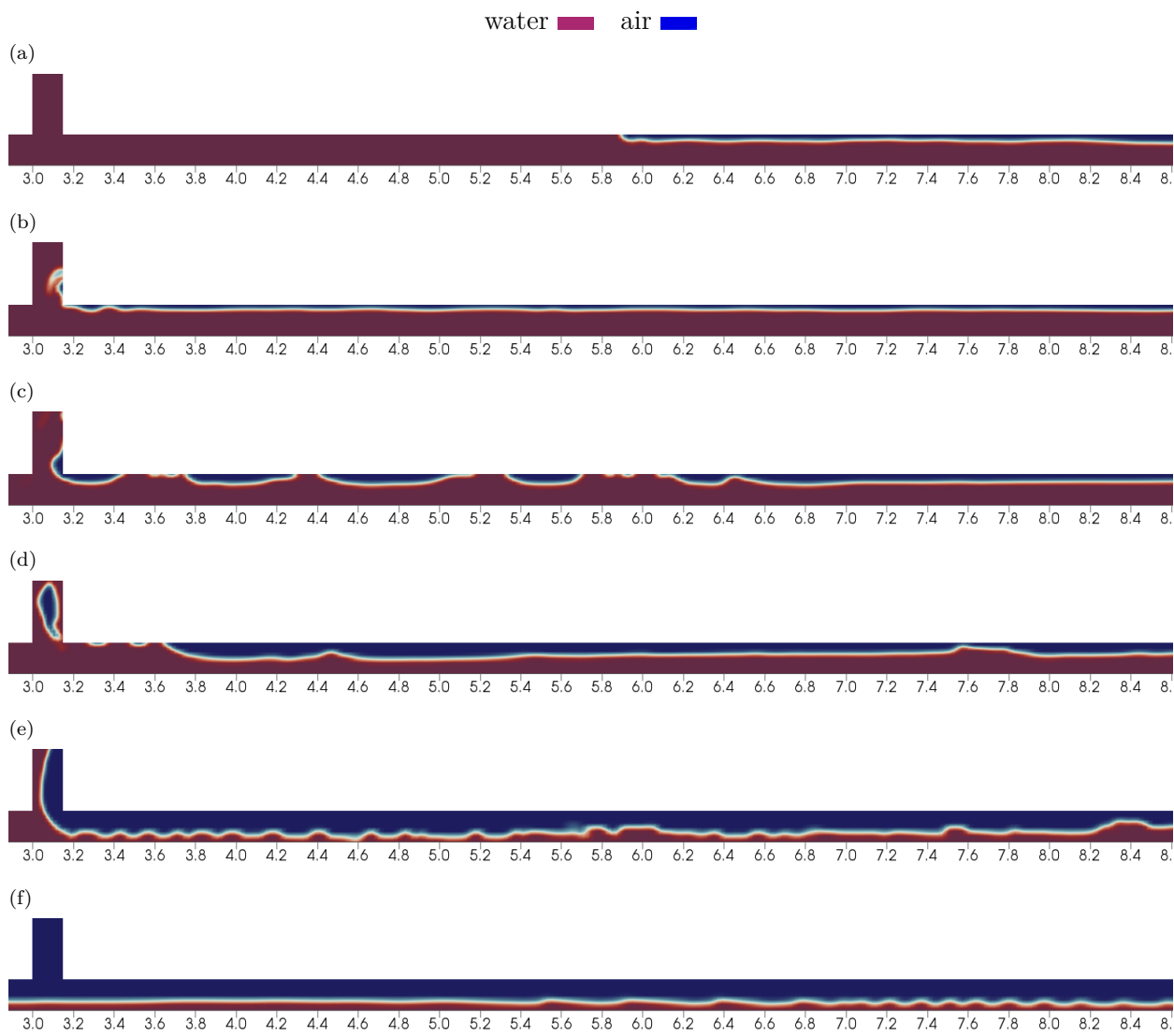


Figure 10 Snapshots of the simulation in the horizontal pipe at (a) $t = 8.0$ s (b) $t = 15.0$ s (c) $t = 18.6$ s (d) $t = 20.0$ s (e) $t = 22.0$ s (f) $t = 32.0$ s (SD=2D, PD=0.05, CW=compressible)

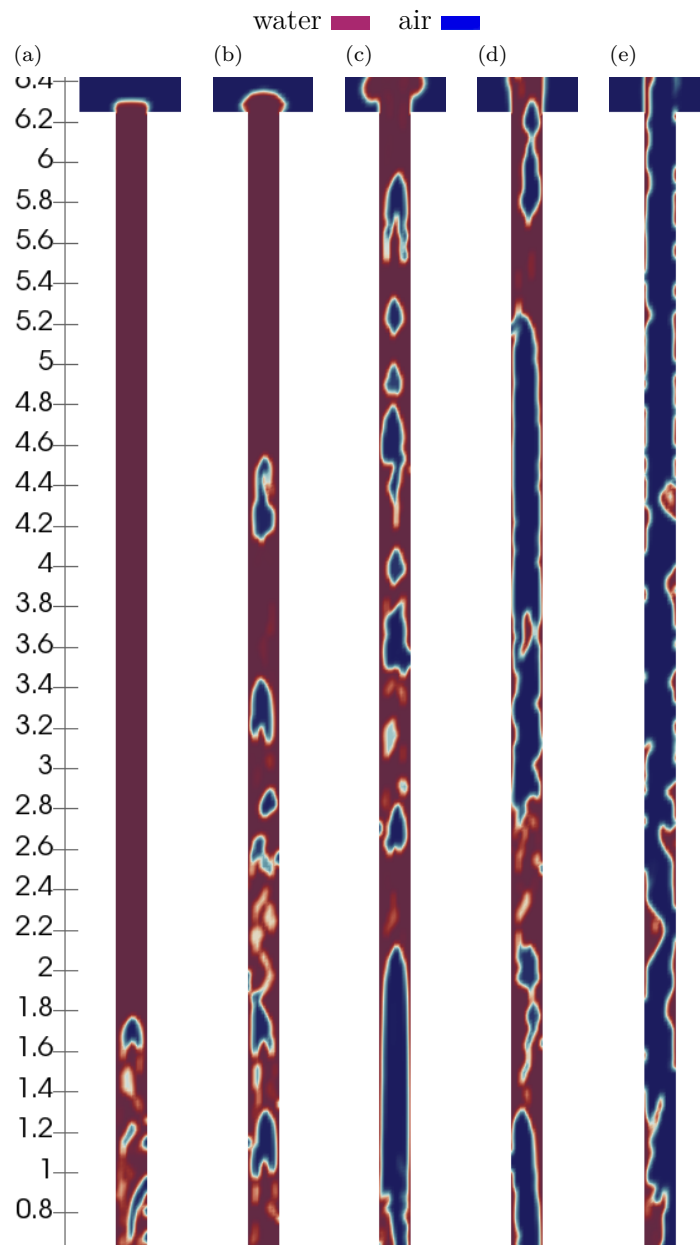


Figure 11 Snapshots of the simulation in the vertical shaft at (a) $t = 18.0\text{ s}$ (b) $t = 20.0\text{ s}$ (c) $t = 20.8\text{ s}$ (d) $t = 21.4\text{ s}$ (e) $t = 22.0\text{ s}$ (SD=2D, PD=0.05, CW=compressible)

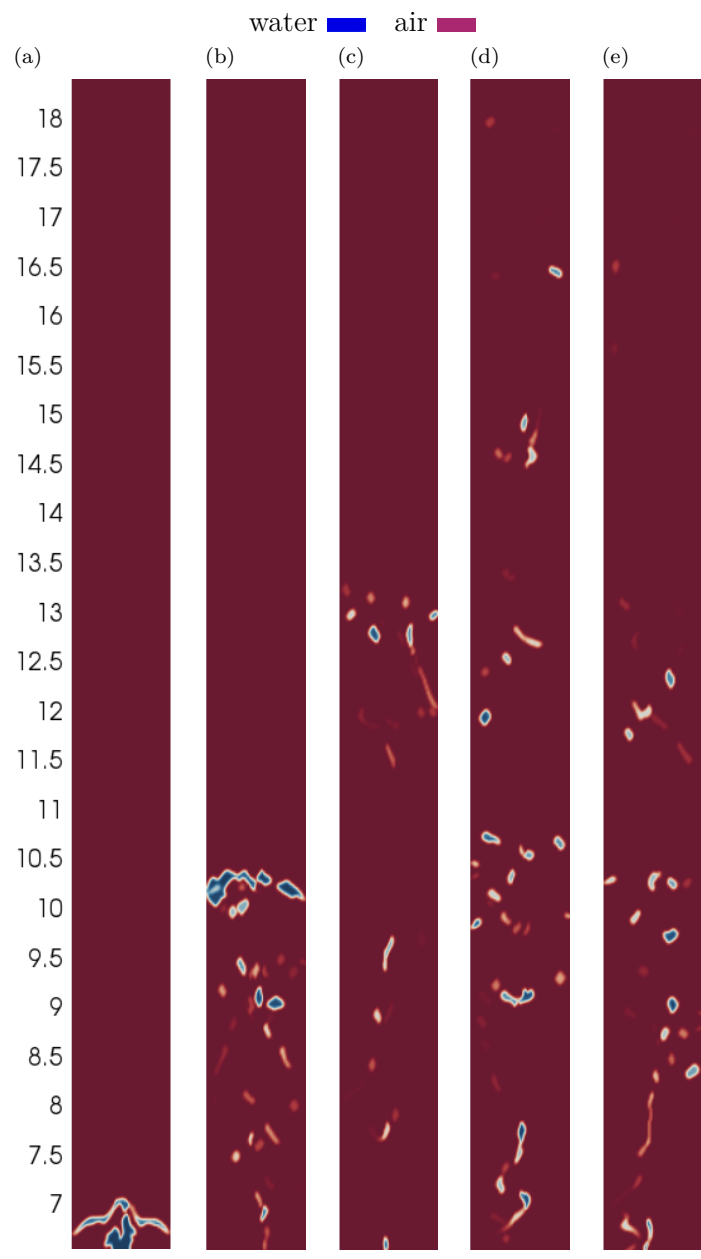


Figure 12 Snapshots of the simulation in the atmospheric domain at (a) $t = 19.6$ s (b) $t = 21.0$ s (c) $t = 21.6$ s (d) $t = 22.9$ s (e) $t = 23.4$ s (SD=2D, PD=0.05, CW=compressible)